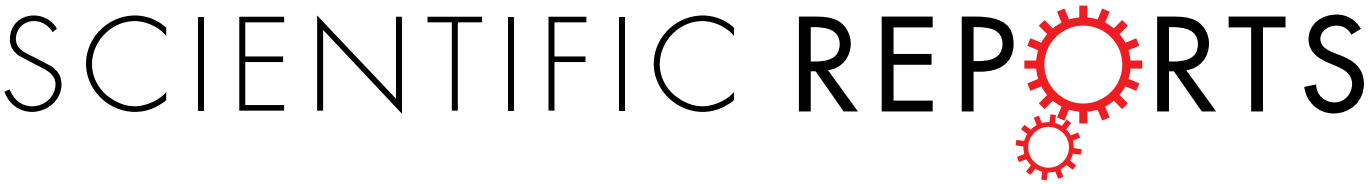

OPEN

Simulation of synaptic short-term plasticity using $Ba(CF_3SO_3)_2$-doped polyethylene oxide electrolyte film

Received: 27 September 2015
Accepted: 30 November 2015
Published: 07 January 2016

C. T. Chang[1,2], F. Zeng[1,2], X. J. Li[1,2], W. S. Dong[1,2], S. H. Lu[1,2], S. Gao[1] & F. Pan[1]

The simulation of synaptic plasticity using new materials is critical in the study of brain-inspired computing. Devices composed of $Ba(CF_3SO_3)_2$-doped polyethylene oxide (PEO) electrolyte film were fabricated and with pulse responses found to resemble the synaptic short-term plasticity (STP) of both short-term depression (STD) and short-term facilitation (STF) synapses. The values of the charge and discharge peaks of the pulse responses did not vary with input number when the pulse frequency was sufficiently low(~1 Hz). However, when the frequency was increased, the charge and discharge peaks decreased and increased, respectively, in gradual trends and approached stable values with respect to the input number. These stable values varied with the input frequency, which resulted in the depressed and potentiated weight modifications of the charge and discharge peaks, respectively. These electrical properties simulated the high and low band-pass filtering effects of STD and STF, respectively. The simulations were consistent with biological results and the corresponding biological parameters were successfully extracted. The study verified the feasibility of using organic electrolytes to mimic STP.

Brain-like computation is studied worldwide to suppress the limitations of the Moore Principle and to construct novel computing technology[1–3]. The determination of elements possessing synapse-like behaviours is a powerful and effective route to realize this target. Researchers have found many materials and devices that mimic synaptic plasticity, including conventional learning protocols, such as the Hebbian learning rule, spike-rate-dependent plasticity (SRDP), spike-timing-dependent plasticity (STDP), long-term plasticity (LTP) and short-term plasticity (STP)[4–19]. However, a material system that can act as the elemental unit of the synapse in artificial neuromorphic circuits has not yet been found. Thus, much research has investigated novel materials with behaviours closely approximating those of bio-synapses.

Recently, systems composed of organic materials have captured the attention of researchers because they possess physical and chemical properties comparable with those of biological systems. In a nanoparticle-doped organic field effect transistor (OFET), the charge/discharge mechanism of a nanoparticle-doped semiconducting polymer[8] was used to simulate excitatory post-synaptic current (EPSC)-like responses and STP-like[15,16,18] behaviour under a frequency-dependent pulse mode. Ionic migration in ionic/electronic hybrid systems was first used by Lai *et al.* to obtain EPSC-like responses and STDP learning protocols[10]. In addition, a double-layer device composed of a semiconducting polymer and a Li-doped electrolyte exhibited frequency selectivity, similar to that of bio-synapses dependent on surface ionic migration; the device responded with depression to low-frequency stimulation (LFS) and with potentiation to high-frequency stimulation (HFS)[20]. Since the plasticity of bio-synapses directly involves the ionic flux crossing the cell membrane, the ionic kinetics in either organic materials or interfaces thereof suggest great versatility in simulating synaptic plasticity[9,20–24]. The selection of certain dopant species in artificial organic materials may provide a system that approximates the behaviours and timing constants of real bio-synapses.

Among many synaptic plasticity properties[15–17,23], STP[15,16,18], which acts as a filter system in biological signal transmission, is crucial in the support of nerve operations[16]. However, studies using memristive systems have not focused on this property, with the exception of that involving a nanoparticle-doped semiconducting polymer[8] and another using solid-state TiO_2 memristor[19]. In the forms and definitions of high band-pass filtering short-term depression (STD)[16], low band-pass filtering short-term facilitation (STF), and the intermediate state

[1]Key Laboratory of Advanced Materials (MOE), School of Materials Science and Engineering, Tsinghua University, Beijing, 100084, People's Republic of China. [2]Centre for Brain Inspired Computing Research (CBICR), Tsinghua University, Beijing 100084, People's Republic of China. Correspondence and requests for materials should be addressed to F.Z. (email: zengfei@mail.tsinghua.edu.cn) or F.P. (email: panf@mail.tsinghua.edu.cn)

between these conditions, STP is characterized by the weight-changed EPSCs[25,26] and controlled by the number of effective neurotransmitter release sites and the concentration of Ca^{2+} in the pre-synapse[16,18,27]. In addition, STP gradually varies with frequency, weight change history, and a persistence time of hundreds of milliseconds[15]. Unlike long-term plasticity (LTP)[17], which has been realized in several nonvolatile memristor devices[28], STP has rarely been achieved in devices, despite its development in several biological computational models[27,29].

In this study, we provided a single-layer salt-doped organic electrolyte film device with polyethylene oxide (PEO), which could be fabricated easily using large-scale engineering processes. The film served as the matrix, while $Ba(CF_3SO_3)_2$ (barium trifluoromethanesulfonate) was used as the salt to simulate the synaptic operating process and the typical band-pass filtering characteristics of STP. Ion-doped organic electrolytes are uncommon in the field of electronics, despite the obvious advantages of easily alternating and mixing ions. The $Ba(CF_3SO_3)_2$-doped PEO responded gradually to saturation with pulse number, and the weight modifications of the charging peaks differed from those of the discharging peaks, indicating distinct band-pass filtering effects. A biological EPSC model of STP proposed in neuroscience[27] was adopted to analyse the pulse responses of the device; characteristic parameters were extracted that were comparable with those of bio-synapses.

Methods

PEO (molecule weight = 100000) and $Ba(CF_3SO_3)_2$ were purchased from Sigma-Aldrich Co. Ltd. and used as without further purification. PEO was dissolved in H_2O to form a 0.4wt% solution with $Ba(CF_3SO_3)_2$ added in the molar ratio of 1:32 with the PEO monomer[20,21]. After dissolution, 3 μL of the $Ba(CF_3SO_3)_2$-PEOsolution was drop-casted on a Pt-deposited Si substrate and baked at 100 °C for 20 min before cooling to room temperature in a N_2-filled glove box. Finally, a 70-nm-thick layer of 300-μm-diameter Pt electrodes were deposited on the substrate by electron beam deposition. The thickness of the $Ba(CF_3SO_3)_2$-doped PEO film was about 0.6 μm (Fig. S1). The electrical characteristics were examined by a semiconductor device analyser (Agilent B1500A) and an arbitrary function generator (Agilent B1530). The direct voltage-current (DC) properties were studied by loading a circular single bias of 0 V → 2 V → 0 V and a double bias of 0 V → 2 V → 0 V → −2 V → 0 V under sweep rates of 1, 10, 50, and 100 V/s. The pulse responses were studied by loading a train of rectangular pulses with 0.5 Vamplitude, 5 ms pulse width, and varied intervals or frequency. Raman spectra of the pure PEO film and the $Ba(CF_3SO_3)_2$-doped PEO electrolyte film were obtained by an HR-800 Raman system with a resolution of 1 cm^{-1}. The excitation source was a 532-nm He-Ne laser. Infrared spectra were recorded with a Vertex 70V Fourier transform infrared (FT-IR) spectrometer at a resolution of 0.4 cm^{-1}.

Results and Discussions

Structural Characterization. The ionic conductivity of PEO-based electrolytes is attributed to ionic migration through the amorphous phase of the PEO matrix, with free cations traversing the polymer backbones through complexation with polar groups and the movement of free anions[30]. Therefore, the amorphous phase of the PEO matrix, cation-polymer complexation, and free ions are vital for the conductivity of the electrolyte. In the photomicrographs shown in Fig. 1, the pure PEO film (Fig. 1a) presents a spherulitic morphology with dendritic lamellae, which indicates a normal polycrystalline structure bridged by amorphous regions[31]. The $Ba(CF_3SO_3)_2$-doped PEO film (Fig. 1b) has an analogous spherulitic morphology with more obscure dendritic lamellae patterns and grain boundaries. This reveals a decrease in lamellae and an increase in amorphous regions compared with the structure of the pure PEO film, which is helpful for the ionic conductivity of the doped polymer.

We examined the cation-polymer interactions by spectrally monitoring the PEO backbone-related bands corresponding to C-O-C, CH_2, CO, CC, and OH groups, and examined the ion-ion associations by monitoring the $\upsilon_s(SO_3)$ and $\delta_s(CF_3)$ bands[30,32] based on the Raman spectra and the IR spectra of the pure PEO and $Ba(CF_3SO_3)_2$-doped PEO films (Fig. 1c,d). based on the Raman and IR spectra of the pure PEO and $Ba(CF_3SO_3)_2$-doped PEO films (Fig. 1c,d). In the Raman spectra (Fig. 1c), the backbone-related bands are slightly shifted and broadened in the spectrum of the doped PEO film compared to the peaks of that of the pure one. In particular, the shift of the D-LAM (disorder-longitudinal acoustic mode) peak at 235.18 cm^{-1} to 238.8cm^{-1} reveals that the cations do interact with the polymer backbones, causing conformational and amorphicity changes[30]. Additional bands at 1033.87cm^{-1} and 756.99 cm^{-1} exhibit the existence of free ions of $\upsilon_s(SO_3)$ and ion pairs of $\delta_s(CF_3)$, respectively[32]. In the IR spectrum of the doped PEO film, compared with that of the unmodified film (Fig. 1d), the band at 1031.87 cm^{-1} shows the existence of $\upsilon_s(SO_3)$ free ions[32], while the 3485.22 cm^{-1} broad band correlating to OH stretching vibrations indicates cation-polymer interactions[33,34]. The 638.41 cm^{-1} band in the finger print region displays a pattern unique to the structure[33,34]. According to this structural analysis, the conductivity of the $Ba(CF_3SO_3)_2$-doped PEO film results from ionic migration through cation-polymer interactions and partial free anions, which constrain the electrical transmission speed and decrease the speed of electric migration. Thus, the macroscopic electrical properties depend on the mode and history of the external field, thus causing the appearance of synaptic plasticity.

Electrical characteristics: DC mode and pulse mode. In the DC sweeping mode, the current routes varying along the external field (E_{ex}) bias cycles do not coincide, and then form mismatching hysteresis loops (Figs. 2a and S2). This is similar to results with inorganic memristors[35]. When loading single biases (Fig. 2a), the loop sequences shift sequentially downward. Along the loop, the current increases with the forward bias, before decreasing with the backward bias through a lower current path. The current path then enters the region of negatively charged currents at a certain voltage threshold, reaching a maximum at 0V. This phenomenon demonstrates the migration and accumulation of Ba^{2+} and $CF_3SO_3^-$ ions at the electrode/electrolyte interface during the forward biases, simultaneously forming polarization layers with an inverted internal field (E_{in})[36]. The E_{in} then gradually offsets the E_{ex}, resulting in negative currents that balance the ionic distribution. As the most non-uniform ionic distribution occurs at 0 V (with the maximum negative current and E_{in}), the E_{ex} of the following bias cycle

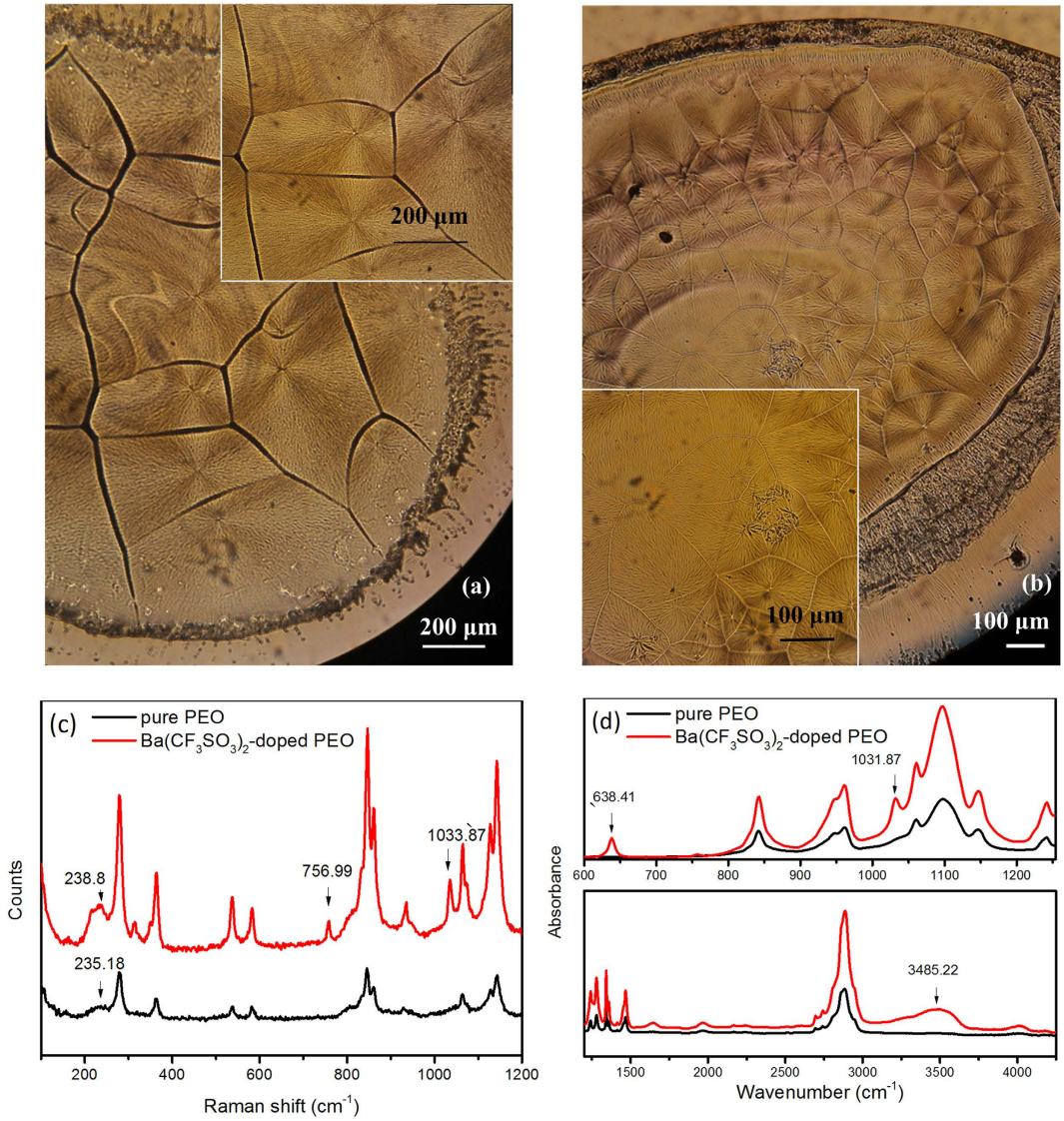

Figure 1. Structural characterization of the electrolyte films. Photomicrographs of (**a**) pure PEO film and (**b**) $Ba(CF_3SO_3)_2$-doped PEO film. (**c**) Raman spectra for pure PEO and $Ba(CF_3SO_3)_2$-doped PEO films. (**d**) FT-IR spectra for pure PEO and $Ba(CF_3SO_3)_2$-doped PEO films.

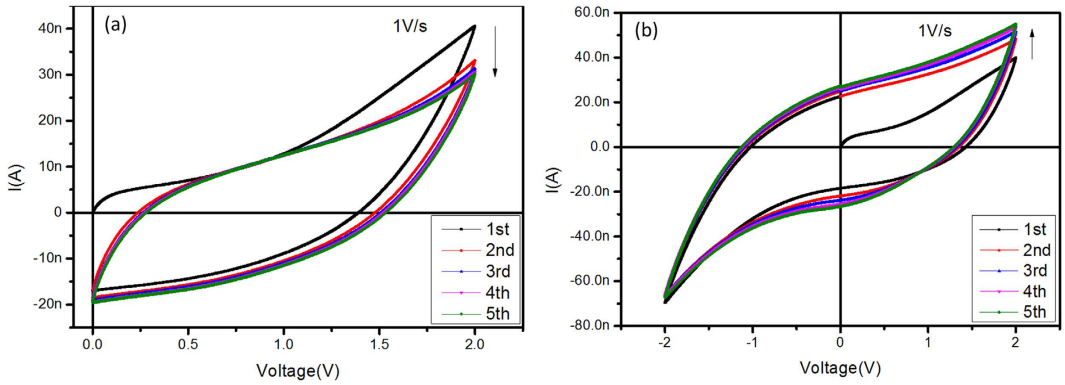

Figure 2. The electrical characterization of the doped PEO film in DC mode. (**a**) Successive single biases of 0 V → 2 V → 0 V … were applied to the device for five cycles. (**b**) Successive double biases of 0 V → 2 V → 0 V → −2 V → 0 V … were applied to the device for five cycles.

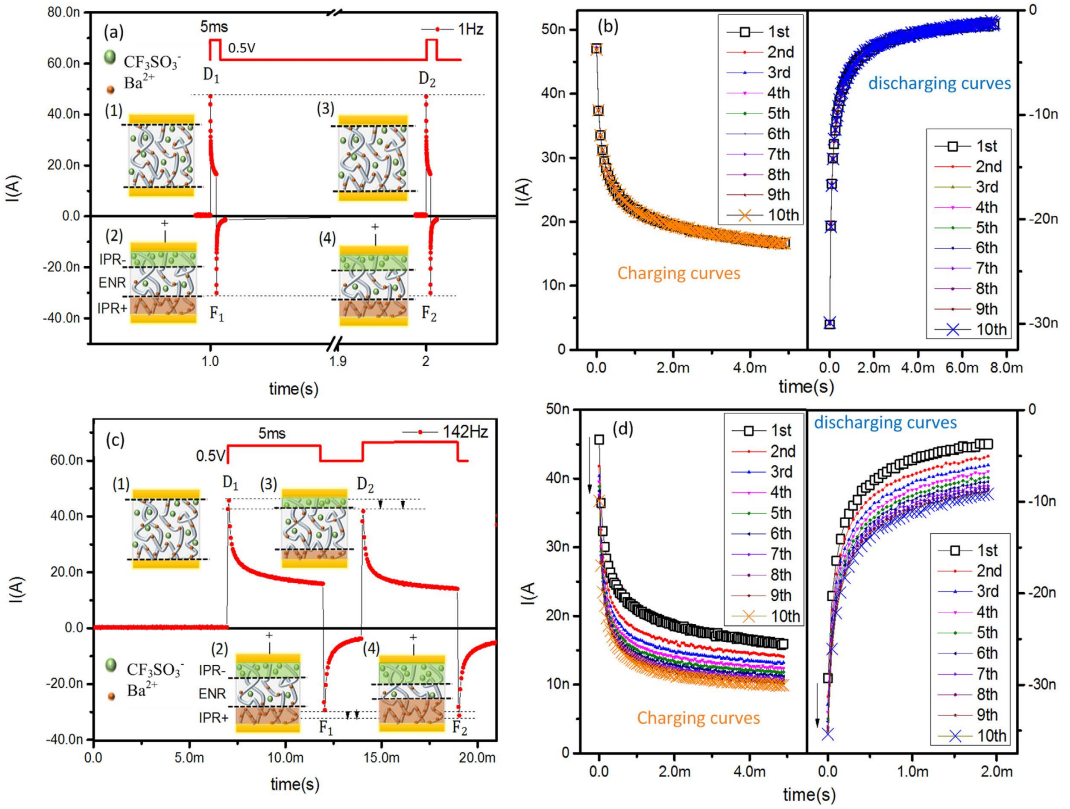

Figure 3. The electrical characterization of the doped PEO film in response to pulsed loads. Rectangular pulses are applied with amplitude of 0.5 V and duration of 5 ms. A train of pulses is loaded to test frequency response of the film. D_i and F_i are charging and discharging peaks for the i^{th} pulse, respectively. (**a**) Under 1 Hz pulse frequency, D_i and F_i sequences remain constant with the pulse number. (1) The initial electric neutral region (ENR) results in D_1. (2) The ionic polar region (IPR) induces F_1. (3) The fully-recovered ENR causes $D_2 = D_1$. (4) The same-sized IPR induces $F_2 = F_1$. (**b**) The charging and discharging curves of the first ten pulse responses under 1 Hz. (**c**) Under 142 Hz pulse frequency (HFS), D_i decreased and F_i increased with increasing *i*. (1) The initial electric natural region (ENR) results in D_1. (2) The ionic polar region (IPR) induces F_1. (3) The partially-recovered ENR results in $D_2 < D_1$. (4) The larger-sized IPR formed by the partially-decayed ENR generates $F_2 > F_1$. (**d**) The charging and discharging curves of the first ten pulse responses at 142 Hz.

should overcome the reserved E_{in}. Therefore, the hysteresis loops shift down and approached a stable-loop state of ionic kinetic balance. When loading double biases (Fig. 2b), the consecutive hysteresis loops are gradually expanded, suggesting that the negative bias not only balances the non-uniform polarization layers of $Ba^{2+}$and $CF_3SO_3^-$ but also further creates an inverted polarized field providing an E_{in} with the same orientation as the positive bias. The narrower hysteresis loops generated at lower voltage sweeping rates suggests a stronger restrictive E_{in} of the polarization layers, caused by the more effective response of the Ba^{2+} and $CF_3SO_3^-$ ions to the E_{ex} (Fig. S2). Overall, the behaviour in DC mode confirms the ionic kinetics of the PEO-based electrolyte.

The electrical characterization with DC mode suggested that the device responded depending on the loading history. It shares a resemblance with the signal handling of informatics and plasticity studies in neuroscience, which were tested under rectangular pulsing modes. Thus, we adopted the same testing approach to examine the exact comparability with our device. In Fig. 3a of LFS pulse mode sketches, a charging peak (D_1) appears at the pulse front and decays gradually to a stable current value within the pulse duration. A discharging peak (F_1) appears at the pulse end and decays gradually to zero. Notably, D_2 and F_2 in Fig. 3a are identical to D_1 and F_1, respectively, as are the charging and discharging curves (Fig. 3b). This demonstrates the state restoration cycles between loading pulses. However, when the interval between consecutive pulses is sufficiently short, as in the HFS shown in Fig. 3c, F_1 does not decay to zero at the next pulse front; the following pulse period begins with a modified state of decreased D_2 and increased F_2, as were the charging and discharging curves (Fig. 3d). F_1 required a full decay period of 0.52 s to provide a restored state of zero for the following load pulses. In addition, the non-volatile effect does not appear, even when the load pulse frequency approaches the limit of 142 Hz (Fig. S3).

In comparing general capacitor and resistor, the response form of our device was similar to that of the R//C device, but with an additional state modification phenomenon in HFS that was not found in the general R//C device (Fig. S4).When searching for connections with capacitance effects, we fitted the charging/discharging curves and found them to match the R//C charging/discharging equations well, with the modification of two capacitance terms of the form A*exp(−t/τ)(Table 1). The time constants τ_1 and τ_2 were nearly equal between

	Charging curves				Discharging curves			
	$I = A_1*\exp(-t/\tau_1) + A_2*\exp(-t/\tau_2) + y_0$				$I = A_1*\exp(-t/\tau_1) + A_2*\exp(-t/\tau_2)$			
	1 Hz	142 Hz			1 Hz	142 Hz		
		1st	5th	9th		1st	5th	9th
y_0	1.657E-08	1.591E-08	1.202E-08	1.043E-08				
A_1	1.825E-08	1.803E-08	1.714E-08	1.711E-08	1.823E-08	1.783E-08	1.869E-08	1.868E-08
τ_1	9.815E-05	9.704E-05	8.612E-05	8.469E-05	9.542E-05	9.923E-05	1.034E-04	1.078E-04
A_2	1.156E-08	1.120E-08	9.238E-09	9.159E-09	1.128E-08	1.091E-08	1.430E-08	1.558E-08
τ_2	1.380E-03	1.380E-03	9.834E-04	9.639E-04	1.520E-03	1.570E-03	2.560E-03	3.020E-03

Table 1. The fitting result of the charging and discharging curves under 1 Hz and 142 Hz.

the 1 Hz pulse response and the first response at 142 Hz. However, they both decreased with increasing pulse number at 142 Hz in the charging curves, but increased in the discharging curves. This implied great influences of the ion pair kinetics (Ba^{2+} and $CF_3SO_3^-$) on the capacitance properties of the device, rather than the electronic conductivity with fast response rates. The hysteretic ionic conductivity may be the core of the state modification phenomenon.

By combining the ionic kinetics results obtained under DC mode, the conductivity and ionic distributions of our device seemed to experience a process under pulsing mode as follows. Initially, the ionic distribution in the $Ba(CF_3SO_3)_2$-doped PEO was uniform, creating an electric neutral region (ENR) without polarity (states labelled (1) in Fig. 3a,c). When a train of rectangular pulses was loaded, D_1 occurred because of the E_{ex}-triggered carrier injection. Meanwhile, the directional migrations of free cations and anions occurred, forming an ionic polar region (IPR) along with E_{in} (states labelled (2) in Fig. 3a,c)[36]. The E_{in} partially screened the E_{ex}-triggered ion migration, causing the current decay throughout the pulse duration. As the pulse ended, the IPR-related E_{in} triggered the inverse discharging peak F_1 and the back-diffusing ionic flux. The latter was weakened by the gradual IPR decay.

The abovementioned back-diffusing ionic flux varied depending on the pulse frequency. In LFS (Fig. 3b), both cations and anions in the PEO matrix fully recovered to the initial state during the pulse interval, resulting in fully recovered ENR and fully decayed IPR (state labelled (3) in Fig. 3a). Thus, the instant carrier injection D_2 evoked by the E_{ex} of the second pulse was equal to D_1. Meanwhile, $F_2$was equal to F_1 because the E_{ex}-triggered ionic relaxation created an equal-sized IPR as that formed in state (2) (state labelled (4) in Fig. 3a). When the frequency was increased (Fig. 3c), the ionic distribution could not fully revert to the initial state, because the pulse interval was insufficient. This generated a partially-recovered ENR and a residual IPR (state (3) in Fig. 3c). Thus, D_2 was a counteractive result of the second E_{ex} and the E_{in} from the residual IPR, causing $D_2 < D_1$. In addition, within the second pulse duration, the IPR was enhanced by the E_{ex}-triggered ionic concentration polarization, thus becoming wider than that evoking F_1, so $F_2 > F_1$ (state (4) in Fig. 3c).

The results in Fig. 3 also suggested that both the charging and discharging peaks D_i and F_i are functions of the pulse number i and the pulse frequency. We can calculate the weight modifications with the formulae $W_{i,f}(D) = I(D_{i,f})/I(D_{1,f})$ and $W_{i,f}(F) = I(F_{i,f})/I(F_{1,f})$, respectively. Here we regard the first pulse responses of either $I(D_{1,f})$ or $I(F_{1,f})$ as the baseline values, because they are unchanged after sufficient intervals between two single pulses. Figure 4 shows the weight modifications of D_i and F_i sequences under the pulse mode. The values of D_i and F_i monotonically decreased and increased, respectively, with pulse number. When the frequency was lower than 80 Hz, the values of D_i and F_i stabilized after a train of 40 pulses. When the frequency exceeded 80 Hz, they were not saturated when the pulse train ended. Notably, the weight amplitude of $D_i$does not match that of F_i. This might suggest the potential for bi-directional signal transmission, although related works were not found among the available neuroscience references.

Interestingly, we found that the weight modifications of D_i and F_i were comparable with those calculated from the EPSCs of the climbing and parallel fibre synapses to the Purkinje cell, (CF) and (PF), respectively[27] (Fig. 4a–d and insets). The former act as low band-pass filters for STD, while the latter acts as high band-pass filters for STF under HFS. Because neural systems usually receive signal packages composed of stimulations at various frequencies[16] (Fig. 4e inset), we randomly selected several inputs to examine the device responses, as shown in Fig. 4e. The resulting weight modifications varied in the same trend as those in Fig. 4a–d and were comparable with the STD and STF of bio-synapses (Fig. 4e inset). This suggested that either the charging or discharging peaks of the $Ba(CF_3SO_3)_2$-doped PEO film could be used to mimic the STP of bio-synapses.

We tested 200 film devices; 95% showed the abovementioned electrical property. Although the level of the weight modification phenomenon was affected by environmental factors such as noise and moisture, testing the devices in approximately the same time period permitted negligible environmental variations. The test results were nearly identical both among different devices and across multiple tests of a single device (Fig. 4e), reflecting the intrinsic properties of the materials and devices.

The simulation of STD and STF. According to the electronic analogies in Figs 3 and 4, we applied the biological EPSC model of STP[27] (equation (1) and (2)) to our device to examine the analogies in ionic kinetics and establish a microscopic basis for mimicking STP. In neural systems, the signal transmission process is both achieved and affected by the state of the pre-synapse, consisting of the number of effective release sites and the Ca^{2+} flux[15,16,18,27,37]. Once the pre-synapse gives trains of stimulations, the Ca^{2+} flux generates numbers of release-ready sites from among the effective sites, thus releasing neurotransmitters and evoking the EPSCs of the

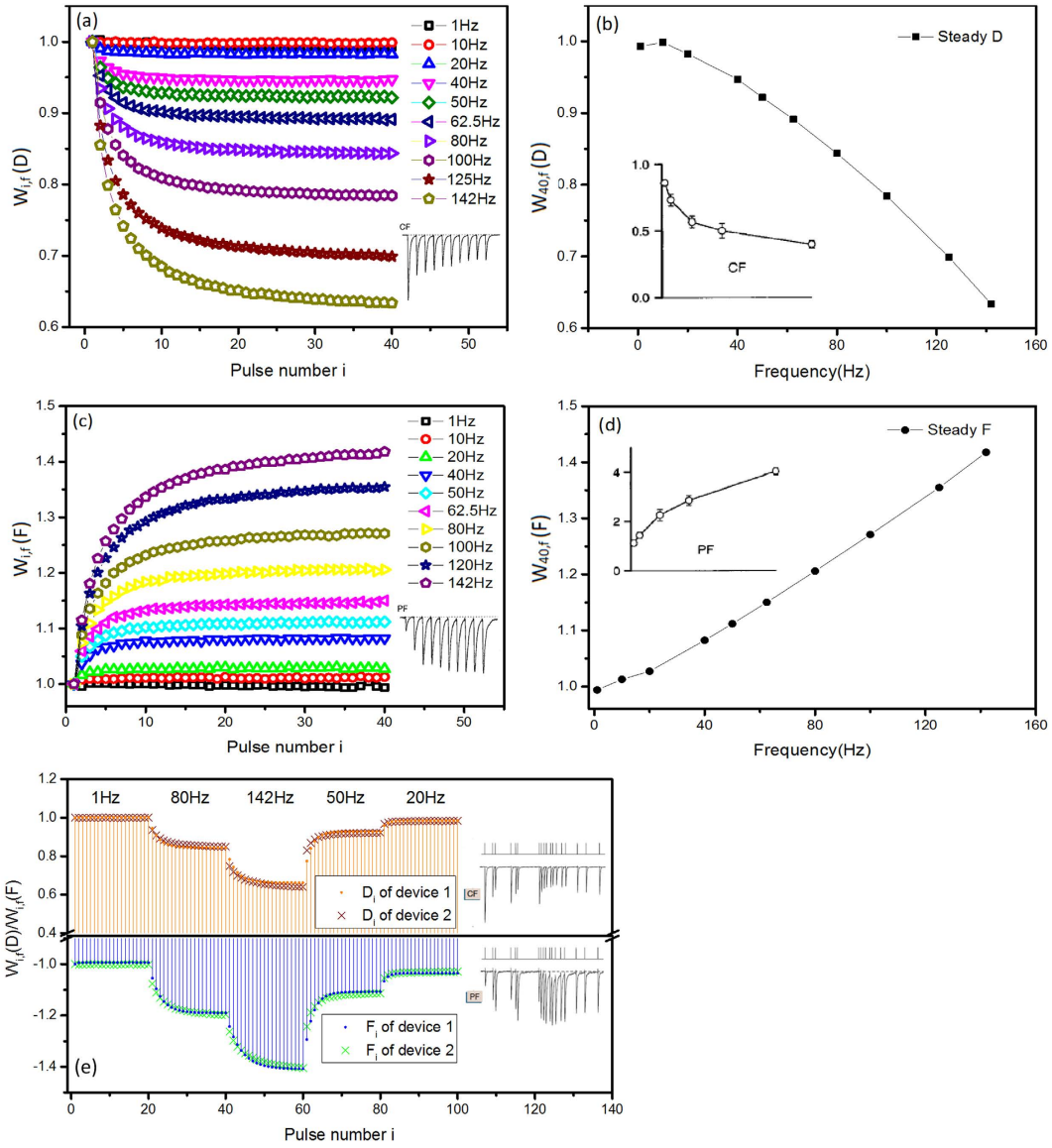

Figure 4. Weight modifications of D_i and F_i sequences under the pulse mode. (**a**) The weight modifications of D_i *vs* pulse number at various frequencies: $W_{i,f}(D) = I(D_{i,f})/I(D_{1,f})$. Inset shows EPSCs of climbing fibre (CF) under HFS, which decreases with increasing pulse number[27]. (**b**) The weight modifications of D_i*vs.* frequency after a train of 40 pulses is loaded; inset shows those of CF:[27] $W_{,n,f}(D) = I(D_{n,f})/I(D_{1,f})$, $n = 40$. (**c**) The weight modifications of F_i*vs.* pulse number at various frequencies: $W_{i,f}(F) = I(F_{i,f})/I(F_{1,f})$. Inset shows EPSCs of parallel fibre (PF) under HFS[27]. (**d**) Weight modifications of F_i*vs.* frequency after a train of 40 pulses is loaded; the inset shows those of PF:[27] $W_{n,f}(F) = I(F_{n,f})/I(F_{1,f})$, $n = 40$. (**e**) A set of D_i and F_i generated by a pulse package containing several frequencies. The results of the two different single devices were tested during the same testing period and showed similar weight modification levels. Insets show EPSC variations of CF and PF in a pulse package containing several frequencies[16].

post-synapse. The release-ready sites become transitionally ineffective after the release process[15,16,27]. During the stimulus interval, the ineffective release sites recover effectiveness and the Ca^{2+} concentration in the pre-synapse decays[15,16,27]. At the moment, the quantity levels are co-decisive to the EPSC variation forms of STP: STD, STF, and the intermediate state in between[15,16].

There are common points between our D_i/F_i sequences in the $Ba(CF_3SO_3)_2$-doped PEO electrolyte film and the STD/STF phenomenon in the bio-synapse: both are influenced by the recovery (ENR/ineffective release sites) and decay (IPR/Ca^{2+}) levels in the stimulus interval. Considering CF, its high release ability makes the recovery level of ineffective release sites dominate the state of the pre-synapse[16]. The effective release sites in the pre-synapse could be simulated as ENR in the device, with EPSCs simulated as D_i. Accordingly, under LFS, the ineffective release sites remaining after release are fully recovered during sufficient stimulus interval and thus able to generate an EPSC of the same level in response to the next stimulus[15,16,18,27], which resembles the fully-recovered ENR generating a constant D_i. Meanwhile, the incomplete recovery level of the ineffective release

N_T	The maximum effective release sites of pre-synapse
	The initial ENR
	The maximum IPR
N	$=N_T * d$, the number of release-ready sites after previous release/previous Ca^{2+}influx
	The residual ENR
	The enhanced IPR
d	The release-ready sites fraction of $N_T$after previous release/ previous Ca^{2+}influx
f	The release fraction/ the decayed Ca^{2+}-caused reduction fraction of N
f_D	*The shrinking fraction of ENR*
f_F	*the decay fraction of IPR*
α	the average amplitude triggered by releasing an effective release site unit
I	$=\alpha * N_T * f(d=1)$, the response intensity delivered by the post-synapse when N_T release
I_D	*The response intensity delivered in the initial ENR state*
I_f	*The response intensity delivered in the maximum IPR state*
k	The recovery/the influx Ca^{2+}-caused enhancement fraction (toward N_T)
k_D	*The recovery fraction (toward initial ENR)*
k_F	*The enhancement fraction (toward maximum IPR)*
t_0	The stimulation moment

Table 2. The characteristic parameters' biological significances and correspondences in the PEO-based electrolyte film.

sites, because the HFS has insufficient stimulus intervals, creates fewer effective release sites to release and generate smaller EPSCs, or weight-decreased STD[15,16,18,27]. This resembles the partially-recovered ENR generating decreasing D_i magnitudes in sequence.

On the other hand, considering PF, its low release ability causes the decay level of $Ca^{2+}$to dominate the state of the pre-synapse[16]. Ca^{2+}, or the release-ready sites yielded by Ca^{2+}, in the pre-synapse could be modelled by IPR in the device, with EPSCs regarded as F_i. Under LFS, the amount of Ca^{2+} in the pre-synapse is fully decayed during sufficient stimulus interval, thus maintaining the same value after the Ca^{2+} influx triggered by the next stimulus is added. Hence, the same numbers of release-ready sites are yielded by this amount of Ca^{2+}, releasing and evoking EPSCs of the samevalue[15,16,18,27]. This process resembles the fully decayed IPR generating constant F_i. Inversely, the incomplete decay level caused by the insufficient stimulus interval in HFS provides additional Ca^{2+} after the next stimulus-triggered Ca^{2+} influx. More release-ready sites are yielded to release, thus generating larger EPSCs, namely weight-increased STF[15,16,18,27]. This process resembles the enhanced IPR based on the partially decayed region generating increasing F_i values in sequence.

The 995 ms pulse interval of the 1 Hz pulse train in our device, which permitted the full recovery of ionic distribution in the PEO matrix, was parallel to the persistence ability of STP within hundreds of milliseconds[15]. Referring to the biological EPSC model of STP[15,16]:

$$\begin{aligned} EPSC &= \alpha * N_T * d * f = \alpha * N * f \\ EPSC(d=1) &= I * f \end{aligned} \tag{1}$$

$$\frac{dd}{dt} = (1-d) * k - d * f * \delta(t_0 - t) \tag{2}$$

we constructed the weight expressions of D_i and F_i sequences as below:

$$\begin{aligned} W_{i,f}(D) &= \alpha * N_i * f_D \\ &= \alpha * \{N_{i-1} - N_{i-1} * f_D + [N_T - N_{i-1} * (1 - f_D)] * k_D\} * f_D \\ &= W_{i-1,f}(D) - W_{i-1,f}(D) * f_D + [I_D - W_{i-1,f}(D) * (1 - f_D)] * k_D \\ &= W_{i-1,f}(D) * (1 - f_D) * (1 - k_D) + I_D * k_D \end{aligned} \tag{3}$$

$$\begin{aligned} W_{i,f}(F) &= \alpha * N_i * f_F \\ &= \alpha * \{N_{i-1} - N_{i-1} * f_F + [N_T - N_{i-1} * (1 - f_D)] * k_F\} * f_D \\ &= W_{i-1,f}(F) - W_{i-1,f}(F) * f_F + [I_F - W_{i-1,f}(F) * (1 - f_F)] * k_F \\ &= W_{i-1,f}(F) * (1 - f_F) * (1 - k_F) + I_F * k_F \end{aligned} \tag{4}$$

$f_D = 0.00277 + 0.001 * \text{frequency}$						
$k_D = 0.174 + 0.511 * \exp(-0.0171 * \text{frequency})$						
$f_F = -(1 - A * k_F)/(1 - k_F) + 1$						
$A = 1.595 - 0.00333 * \text{frequency}$						
$k_F = 0.213 + 0.319 * \exp(-0.0354 * \text{frequency})$						
	I_D	f_D	k_D	I_F	f_F	k_F
1 Hz	1	0.0038	0.676	1.582	0.643	0.521
10 Hz		0.013	0.604		0.435	0.437
20 Hz		0.023	0.537		0.310	0.370
40 Hz		0.043	0.432		0.189	0.290
50 Hz		0.053	0.391		0.156	0.267
62.5 Hz		0.065	0.349		0.127	0.248
80 Hz		0.083	0.304		0.099	0.231
100 Hz		0.103	0.266		0.075	0.222
125 Hz		0.128	0.234		0.050	0.216
142 Hz		0.145	0.219		0.034	0.215

Table 3. The fitting result obtained from fittingexpressions (3) and (4) to the D_i and F_i sequences in Fig. 3a,c.

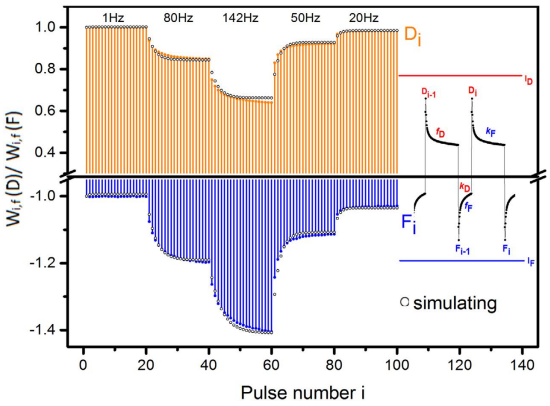

Figure 5. The simulating result of Fig. 4e; the inset shows the parameters in the weight expressions of the D_i and F_i sequences (equations (3) and (4)).

Briefly, because the biological EPSC equations (1) and (2) possess history-based features, the derivative equations (3) and (4) are recursive functions for D_i and F_i. The characteristic parameters f_D and k_D are the shrinking and recovery ratios, respectively, of ENR, which correspond to the f (release ratio) and k (recovery ratio) of effective release sites. I_D is, on behalf of the weight of D_i, generated by the maximum ENR, with I, on behalf of the EPSC, generated by the maximum effective release sites. The characteristic parameters f_F and k_D are the reduction and enhancement ratios, respectively of the IPR, corresponding to f (decay ratio) and k (influx ratio) of Ca^{2+}-caused release-ready sites (Ca^{2+}). I_F is, on behalf of the weight of F_i, generated by the maximum IPR, while I is generated by the maximum number of Ca^{2+}-caused release-ready sites on behalf of the EPSC. The details of the biological significance contrasted with the parameters are shown in Table 2[15,16,27]. Among the parameters, f_D, k_D, f_F, and k_D are in the range of (0,1] and are functions of frequency; D_1 and F_1 are set as 1; $I_D = 1$; $I_F > 1$;D_i diverges from I_D and F_i approaches I_F (Fig. 4 inset)[15,16,27]. The values of the parameters f_D, k_D, f_F, k_D, and I_F were obtained by fitting equations (3) and (4) to the D_i and F_i sequences in Fig. 4a,c (Table 3), which were affected by the salt type and salt concentration in the PEO-based electrolyte film, the thickness of the film, and the depth to which the test probe was inserted, because of the elasticity of the PEO matrix.

The variation trends of f_D and f_F were comparable with the biological parameter f. It appeared that higher pulse frequencies correlated to larger f_D values. This agreed with CF's high release ability (f) of the effective release sites that caused STD, which grew and acted more intensively at stronger HFS[15,16,27], as shown in Fig. 4b and the inset. On the contrary, higher pulse frequencies correlated to smaller values of f_F, which also agreed with PF's low release ability (f), namely the low reduction degree of Ca^{2+}-caused release-ready sites, which decreased and caused more intensive STF in stronger HFS[15,16,27], as shown in Fig. 4d and the inset. Based on the characteristic parameters in Table 3, the simulating results of equations (3) and (4) agreed well with the $W_{i,f}$ (D) and $W_{i,f}$ (F) in Fig. 4e as shown in Fig. 5, supporting not only the fitting result but the feasibility of simulating STP with the $Ba(CF_3SO_3)_2$-doped PEO electrolyte film device.

Notably, according to the unidirectional signal transmission in neural systems, the D_i and F_i of the single device unit cannot be seen as EPSCs simultaneously because they have opposite peak directions. Thus, in neural system-like device integrations containing several elemental device units (or simulated synapses), only the response peaks sharing peak directions can be regarded as single simulation systems. With this limitation, our device can only simulate the interactions of STPs or STDs themselves, rather than those in between, as the bio-synapse network does. Thus, to broaden the future applications of device integration, other devices which conversely manifest STF in charging peaks and STD in discharging peaks must be designed by fabricating different materials into layered structures[5,7,20,38–40]. From another perspective, without restricting the peaks to unidirectional EPSCs, the idea of "feedback plasticity" was introduced, which illustrated the process of the post-synapse inversely transmitting signals to the pre-synapse to inhibit the release of release sites[16]. Accordingly, the opposing D_i and F_i signals can be applied simultaneously in a single simulation system, on behalf of either EPSCs or feedbacks. For example, F_i could be regarded as the feedback signals, simulating the depression of EPSCs (D_i). However, as the feedback plasticity phenomenon is not yet well understood biologically, we cannot know if the exact forms of the feedback signals are identical to F_i. Hence, this biological phenomenon must be further studied before being applied to the development of computational models and simulation devices.

Conclusions

Devices fabricated from $Ba(CF_3SO_3)_2$-doped PEO film using the phenomenon of internal ionic relaxation-related back-diffusion are feasible materials to simulate STP[15,16,18,27]. The values of the charging and discharging peaks of the pulse responses did not vary with the input number when the pulse frequency was sufficiently low at 1 Hz. However, the peaks decreased or increased gradually, achieving stable values with increased input numbers at increased frequencies. The weight modification, calculated based on these stable values, varied with the input frequency, resulting in the depression and potentiation of the charging and discharging peaks, respectively. According to these electrical properties, we simulated STD and STF of two bio-synapse types, which manifested high band-pass filtering and low band-pass filtering effects, respectively. The simulations were consistent with biological results and corresponding biological parameters were successfully extracted. Our study suggests the possibility of ion-dependent simulations of STP.

References

1. Service, R. F. The brain chip. *Science* **345,** 614–616 (2014).
2. Prezioso, P. *et al.* Training and operation of an integrated neuromorphic network based on metal-oxide memristors. *Nature* **521,** 61–64 (2015).
3. Indiveri, G., Chicca, E. & Douglas, R. A VLSI array of low-power spiking neurons and bistable synapses with spike-timing dependent plasticity. *IEEE Trans. Neural Networks* **17,** 211–221 (2006).
4. Chang, T., Jo, S. H. & Lu, W. Short-term memory to long-term memory transition in a nanoscale memristor. *ACS Nano* **5,** 7669–7676 (2011).
5. Li, S. Z. *et al.* Synaptic plasticity and learning behaviours mimicked through Ag interface movement in an Ag/conducting polymer/Ta memristive system. *J. Mater. Chem. C* **1,** 5292–5298 (2013).
6. Jeong, D. S., Kim, I., Ziegler, M. & Kohlstedt, H. Towards artificial neurons and synapses: a materials point of view. *RSC Adv*. **3,** 3169–3183 (2013).
7. Zeng, F., Li, S. Z., Yang, J., Pan, F. & Guo, D. Learning processes modulated by the interface effects in a Ti/conducting polymer/Ti resistive switching cell. *RSC Adv*. **4,** 14822 (2014).
8. Alibart, F. *et al.* An organic nanoparticle transistor behaving as a biological spiking synapse. *Adv. Funct. Mater.* **20,** 330–337 (2010).
9. Kim, S. *et al.* Experimental Demonstration of a Second-Order Memristor and Its Ability to Biorealistically Implement Synaptic Plasticity. *Nano Lett.* **15,** 2203–2211 (2015).
10. Lai, Q. X. *et al.* Ionic/Electronic Hybrid Materials Integrated in a Synaptic Transistor with Signal Processing and Learning Functions. *Adv. Mater.* **22,** 2448–2453 (2010).
11. Josberger, E. E., Deng, Y. X., Sun, W., Kautz, R. & Rolandi, M. Two-Terminal Protonic Devices with Synaptic-Like Short-Term Depression and Device Memory. *Adv. Mater.* **26,** 4986–4990 (2014).
12. Pickett, M. D., Medeiros-Ribeiro, G. & Williams, R. S. A scalable neuristor built with Mott memristors. *Nature Mater*. **12,** 114–117 (2013).
13. He, W. *et al.* Enabling an Integrated Rate-temporal Learning Scheme on Memristor. *Sci. Rep*. **4,** 4755 (2014).
14. Li, Y. *et al.* Ultrafast Synaptic Events in a Chalcogenide Memristor. *Sci. Rep.* **3,** 1619 (2013).
15. Zucker, R. S. & Regehr, W. G. Short-term synaptic plasticity. *Annu. Rev. Physiol.* **64,** 355–405 (2002).
16. Abbott, L. F. & Regehr, W. G. Synaptic computation. *Nature* **431,** 796 (2004).
17. Lever, C., Wills, T., Cacucci, F., Burgess, N. & O'Keefe, J. Long-term plasticity in hippocampal place-cell representation of environmental geometry. *Nature* **416,** 90–94 (2002).
18. Byrne, J. H. & The University of Texas Health Science Center at Houston (UTHealth). *Chapter 7: Synaptic Plasticity. Neuroscience*. (1997) Available at: http://neuroscience.uth.tmc.edu/s1/chapter07.html. (Accessed: 30th June 2015).
19. Berdan, R. *et al.* Emulating short-term synaptic dynamics with memristive devices. arXiv preprint arXiv:1507.02066 (2015).
20. Zeng, F., Lu, S. H., Li, S. Z., Li, X. J. & Pan, F. Frequency Selectivity in Pulse Responses of Pt/Poly(3-Hexylthiophene-2,5-Diyl)/Polyethylene Oxide + Li^+/Pt Hetero-Junction. *PLoS ONE* **9,** e108316 (2014).
21. Lu, S. H. *et al.* Controlling Ion Conductance and Channels to Achieve Synaptic-like Frequency Selectivity. *Nano-Micro Lett*. **7,** 121–126 (2015).
22. Dong, W. S. *et al.* Frequency-dependent learning achieved using semiconducting polymer/electrolyte composite cells. *Nanoscale* **7,** 16880–16889 (2015).
23. G. Rachmuth, H. Z. Shouval, M. F. Bear & Poon, C. S. A biophysically-based neuromorphic model of spike rate- and timing-dependent plasticity. *PNAS* **108,** E1266–E1274 (2011).
24. Du, C., Ma, W., Chang, T., Sheridan, P. & Lu, D. W. Biorealistic Implementation of Synaptic Functions with Oxide Memristors through Internal Ionic Dynamics. *Adv. Funct. Mater.* **25,** 4290–4299 (2015).
25. Dudek, S. M. & Bear, M. F. Homosynaptic long-term depression in area CA1 of hippocampus and effects of N-methyl-D-aspartate receptor blockade. *PNAS* **89,** 4363–4367 (1992).

26. Bi, G. Q. & Poo, M. M. Synaptic modification in cultured hippocampal neurons: dependence on spike timing, synaptic strength and postsynaptic cell type. *J. Neurosci.* **15,** 10464–10472 (1998).
27. Dittman, J. S., Kreitzer, A. C. & Regehr, W. G. Interplay between facilitation, depression, and residual calcium at three presynaptic terminals. *J. Neurosci.* **20,** 1374–1385 (2000).
28. Jo, S. H. *et al.* Nanoscale memristor device as synapse in neuromorphic systems. *Nano Lett.* **10,** 1297–1301 (2010).
29. David L. B. & David T. Yue. Release-Independent Short-Term Synaptic Depression in Cultured Hippocampal Neurons,. *J. Neurosci.* **20,** 2480–2494 (2000).
30. Chaurasia, S. K., Singh, R. K. & Chandra, S. Ion–polymer complexation and ion-pair formation in a polymer electrolyte PEO: LiPF 6 containing an ionic liquid having same anion: A Raman study. *Vibrational Spectroscopy* **68,** 190–195 (2013).
31. You, J. W., Chiu, H. J. & Don, T. M. Spherulitic morphology and crystallization kinetics of melt-miscible blends of poly (3-hydroxybutyrate) with low molecular weight poly (ethylene oxide). *Polymer* **44,** 4355–4362 (2003).
32. Rhodes, C. P. & Frech, R. Cation–anion and cation–polymer interactions in (PEO) n $NaCF_3SO_3$ (n = 1–80). *Solid State Ionics* **121,** 91–99 (1999).
33. ChemAnalytical LLC., *FT-IR Services at ChemAnalytical. ChemAnalytical.* (2010) Available at: http://www.chemanalytical.com/ft-ir-spectra. (Accessed: 10th June 2015).
34. Merlic, C. A. & Fam, B. C. & The Regents of University of California., *Introduction to IR Spectra*. *Webspectra.* (1997) Available at: http://www.chem.ucla.edu/~webspectra/irintro.html. (Accessed: 30th June 2015).
35. Strukov, D. B. & Williams, R. S. Exponential ionic drift: fast switching and low volatility of thin-film memristors. *Appl Phys A* **94,** 515–519 (2009).
36. Valov, I. *et al.* Nanobatteries in redox-based resistive switches require extension of memristor theory. *Nat. Commun.* **4** 1771 (2013).
37. Bear, M. F., Cooper, L. N. & Ebner, F. F. A physiological basis for a theory of synapse modification. *Science* **237,** 42–48 (1987).
38. Wang, Z. S., Zeng, F., Yang, J., Chen, C. & Pan, F. Resistive switching induced by metallic filaments formation through poly (3, 4-ethylene-dioxythiophene): poly (styrenesulfonate). *ACS Appl. Mater. & Interfaces* **4,** 447–453 (2012).
39. Wang, Z. S. *et al.* Reproducible and controllable organic resistive memory based on Al/poly(3,4-ethylene-dioxythiophene):poly(styrenesulfonate)/Al structure. *Appl. Phys. Lett.* **97,** 253301 (2010).
40. Yang, J. *et al.* Modulating resistive switching by diluted additive of poly (vinylpyrrolidone) in poly (3, 4-ethylenedioxythiophene): poly (styrenesulfonate). *J. Appl. Phys.* **110,** 114518 (2011).

Acknowledgements

This work was supported by National Natural Science foundation of China (Grant Nos 51231004 and 51371103) and National Hi-tech (R&D) project of China (Grant Nos 2013AA030801) and Brain Inspired Computing Research, Tsinghua University (20141080934).

Author Contributions

C.T.C. finished experiments, wrote the paper and F.Z. designed the experiments and wrote the paper. X.J.L., W.S.D. and S.H.L. assisted on structural analysis and electronic characterization. S.G. and F.P. discussed the experiments.

Additional Information

Supplementary information accompanies this paper at http://www.nature.com/srep

Competing financial interests: The authors declare no competing financial interests.

How to cite this article: Chang, C. T. *et al.* Simulation of Synaptic Short-term Plasticity using $Ba(CF_3SO_3)_2$-doped polyethylene oxide electrolyte film. *Sci. Rep.* **6**, 18915; doi: 10.1038/srep18915 (2016).